Structural and dynamic changes in P-Rex1 upon activation by PIP_3 and inhibition by IP_4

Sandeep K. Ravala[1], Sendi Rafael Adame-Garcia[2], Sheng Li[3], Chun-Liang Chen[1], Michael A. Cianfrocco[4], J. Silvio Gutkind[2], Jennifer N. Cash*[5], and John J. G. Tesmer*[1]

[1]Departments of Biological Sciences and of Medicinal Chemistry and Molecular Pharmacology, Purdue University, West Lafayette, Indiana 47907, United States

[2]Department of Pharmacology and Moores Cancer Center, University of California, San Diego, San Diego, CA 92093, USA

[3]Department of Medicine, University of California San Diego, La Jolla, CA 92093, USA.

[4]Department of Biological Chemistry, University of Michigan, Ann Arbor, Michigan 48109, United States

[5]Department of Molecular and Cellular Biology, University of California-Davis, Davis, CA, 95616, USA.

*To whom correspondence should be addressed: jcash@ucdavis.edu and jtesmer@purdue.edu

Abstract

PIP_3-dependent Rac exchanger 1 (P-Rex1) is abundantly expressed in neutrophils and plays central roles in chemotaxis and cancer metastasis by serving as a guanine nucleotide exchange factor (GEF) for Rac. The enzyme is synergistically activated by PIP_3 and the heterotrimeric Gβγ subunits, but mechanistic details remain poorly understood. While investigating the regulation of P-Rex1 by PIP_3, we discovered that Ins(1,3,4,5)P_4 (IP_4) inhibits P-Rex1 activity and induces large decreases in backbone dynamics in diverse regions of the protein. Cryo-electron microscopy analysis of the P-Rex1·IP_4 complex revealed a conformation wherein the pleckstrin homology (PH) domain occludes the active site of the Dbl homology (DH) domain. This configuration is stabilized by interactions between the first DEP domain (DEP1) and the DH domain and between the PH domain and a 4-helix bundle (4HB) subdomain that extends from the C-terminal domain of P-Rex1. Disruption of the DH–DEP1 interface in a DH/PH-DEP1 fragment enhanced activity and led to a more extended conformation in solution, whereas mutations that constrain the occluded conformation led to decreased GEF activity. Variants of full-length P-Rex1 in which the DH–DEP1 and PH–4HB interfaces were disturbed exhibited enhanced activity during chemokine-induced cell migration, confirming that the observed structure represents the autoinhibited state in living cells. Interactions with PIP_3-containing liposomes led to disruption of these interfaces and increased dynamics protein-wide. Our results further suggest that inositol phosphates such as IP_4 help to inhibit basal P-Rex1 activity in neutrophils, similar to their inhibitory effects on phosphatidylinositol-3-kinase.

Introduction

Localized activation of signaling is required for proper cell migration. Phosphatidylinositol 3,4,5-trisphosphate (PIP_3)-dependent Rac exchanger 1 (P-Rex1) is a Rho guanine nucleotide exchange factor (RhoGEF) abundantly expressed in neutrophils that mediates chemotaxis and the generation of reactive oxygen species via activation of Rac GTPases (Dorseuil et al., 1992). The protein is comprised of a catalytic Dbl homology (DH) domain followed by a pleckstrin homology (PH) domain, two DEP domains (DEP1 and DEP2), two PDZ domains (PDZ1 and PDZ2), and a C-terminal inositol polyphosphate-4-phosphatase-like (IP4P) domain (Fig. 1A).

P-Rex1 exhibits low basal activity until it becomes activated via direct interaction with membrane-bound regulators PIP_3 and Gβγ which act synergistically (Cash et al., 2019, 2016; Mayeenuddin et al., 2006; Welch et al., 2002), indicating that they use distinct modes of regulation. Although relatively little is known about how P-Rex1 transitions to an activated state, recent structural studies have defined their docking sites. Gβγ engages a scaffold composed of an amalgamation of the DEP2-PDZ1-PDZ2-IP4P domains and likely helps recruit P-Rex1 to the cell membrane (Cash et al., 2019). In contrast, PIP_3 binds to the PH domain (Hill et al., 2005) in a basic pocket (Cash et al., 2016), but this is not necessary for its recruitment to the cell membrane, implying that PIP_3 instead induces a conformational change that activates the enzyme (Cash et al., 2016). Because domains C-terminal to the catalytic DH domain are well known to be involved in autoinhibition (Chávez-Vargas et al., 2016; Hill et al., 2005; Ravala et al., 2020; Urano et al., 2008), the allosteric change induced by PIP_3 must defeat interdomain contacts and render the catalytic DH domain accessible to its substrate.

Here, we used hydrogen-deuterium exchange mass spectrometry (HDX-MS), cryo-electron microscopy (cryo-EM) single particle analysis (SPA), and small-angle X-ray scattering

(SAXS) along with functional studies and live cell experiments to show that activation of P-Rex1 involves disruption of two different inhibitory interfaces between domains across the length of the protein. Surprisingly, we found that the PIP_3 headgroup analog IP_4 can reduce P-Rex1 activity by stabilizing the autoinhibited conformation of the enzyme at physiologically relevant concentrations, suggesting a previously unknown, additional mechanism of regulation. Our experiments further suggest that P-Rex1 binding to PIP_3-containing membranes induces conformational changes that unwind P-Rex1 into a fully active state.

Results

IP_4 induces protection from deuterium incorporation on regions of P-Rex1 distal from the PIP_3-binding site.

Previous work suggested that PIP_3 binding to the PH domain activates P-Rex1 purely through an allosteric mechanism (Cash et al., 2016). Thus, we anticipated that binding of the soluble headgroup of PIP_3, IP_4, to full-length P-Rex1 could also lead to conformational changes characteristic of the activated state. To test this, we analyzed P-Rex1 in the presence and absence of IP_4 using HDX-MS. We observed strong protection from deuterium incorporation in the PIP_3-binding site on the PH domain in the presence of IP_4 (Fig. 1A&B, Sup. Data 1). However, we also observed strong protection in other regions of the protein: namely on the surface of the PH domain, particularly in the β5/β6 loop, and in several regions within an extension of the C-terminal IP4P domain that was not visualized in the P-Rex1–Gβγ complex (Fig. 1A&C) (Cash et al., 2019). We speculated that these diverse regions form more stable long-range interactions in the presence of IP_4.

IP_4 allosterically inhibits P-Rex1.

Based on our HDX-MS data, we hypothesized that IP_4 could inhibit activity of full-length P-Rex1. Using an *in vitro* GEF activity assay on soluble Cdc42 in the presence of liposomes, we observed that IP_4 inhibits PIP_3-mediated activation of P-Rex1 with an IC_{50} value of 1.4 μM (Fig. 1D). Competition was not observed with $Ins(1,4,5)P_3$, indicating that inhibition is dependent on the 3-phosphate, which is critical for PIP_3 binding to the P-Rex1 PH domain (Cash et al., 2016). However, IP_4 did not affect the activity of the P-Rex1 DH/PH or DH/PH-DEP1 fragments (Sup. Fig. 1A&B). Collectively, these results indicated that IP_4 inhibits P-Rex1 allosterically and that this inhibition is dependent on long range interactions between the regions shown to be protected by IP_4 in the Gβγ-binding scaffold (DEP2-PDZ1-PDZ2-IP4P) and in the DH/PH-DEP1 module.

IP_4 stabilizes long-range interactions mediated by the P-Rex1 DEP1 and PH domains.

To understand the molecular basis of IP_4-mediated stabilization and inhibition, we analyzed full-length P-Rex1 with and without IP_4 using cryo-EM SPA (Sup. Fig. 2A). Initial datasets were collected using a Glacios transmission electron microscope and then processed through 2D classification (Sup. Fig. 2B-D). In both datasets, most classes showed only the Gβγ-binding core of P-Rex1 (Sup. Fig. 2C&D). A few classes contained particles with additional mass to the side of the core, close to the PDZ or DEP domains (Sup. Fig. 2C, orange boxes). This mass could represent either the N-terminal domains or another P-Rex1 particle in proximity. Only in the sample containing IP_4 could we observe class averages with additional mass next to the core opposite the side that binds Gβγ (Sup. Fig. 2D, green boxes). Based on its size, location, our HDX-MS data (Fig. 1), and low-resolution maps of P-Rex1 generated in a previous study (Cash et al., 2019), this

mass most likely corresponded to the N-terminal DH/PH-DEP1 domains interacting with an elongated subdomain extending from the IP4P domain.

We next collected much larger datasets on the P-Rex1·IP_4 complex using a Krios transmission electron microscope and determined the structure of this complex at an average resolution of 4.1 Å (Fig. 2A-B, Table 1, and Sup. Fig. 3). Similar to the P-Rex1–Gβγ complex (Cash et al., 2019), this sample exhibited a preferred orientation on grids, necessitating the addition of data collected on a tilted sample (Sup. Fig. 3A, C). The resulting 3D reconstruction clearly shows the Gβγ-binding core, composed of DEP2, PDZ1, PDZ2, and the majority of the IP4P domain, from which there are two extensions of density that contact one another to form a loop-like structure (Fig. 2A and Sup. Fig. 3D). One extension corresponds to a large insertion in the IP4P domain that contains IP_4-stabilized regions (Fig. 1) and that was disordered in the P-Rex1–Gβγ complex (Cash et al., 2019). The ordered elements of the insertion form a long 4-helix bundle (4HB) most similar in fold to focal adhesion targeting (FAT) domains (Hayashi et al., 2002), which are found in other peripheral membrane proteins involved in cell adhesion and migration. The other extension corresponds to the DH/PH-DEP1 domains. Based on its distinct shape, the PH domain (Cash, 2016) was fit into density along the side of the 4HB. The position of the DH domain was also obvious, but individual helices of the DH domain were lower in resolution and more dynamic relative to the rest of the structure (Sup. Fig. 3D). The relative positions of the DH and PH domains mandate a severe bend in the helix connecting the DH and PH domains (Fig. 2A&B), resulting in a jack-knifed configuration of the DH/PH module that blocks access to the GTPase binding site on the DH domain. The remaining mass, immediately adjacent to the end of the DH domain opposite its N-terminus, corresponds to DEP1. Using the required connectivity of its N- and C-termini to the PH and DEP2 domains, respectively, DEP1 was docked in a manner that

129 complemented residues on the DH domain and corroborated the HDX-MS data (Sup. Fig. 4). Weak
130 density corresponding to a long 5-turn extension of the αC helix of the PH domain connects to the
131 N-terminus of DEP1, but its C-terminal connection to DEP2 is disordered, likely explaining lower
132 local resolution in the DEP1 region (Sup. Fig. 3D). Overall, the conformation of the P-Rex1 Gβγ-
133 binding core is essentially the same as in the P-Rex1–Gβγ complex (RMSD deviation of 1.1 Å for
134 701 Cα atoms).

135 The contact between the PH domain and the 4HB is primarily mediated via the β1 and β2
136 strands and β5/β6 loop of the PH domain (Fig. 2C&D). In all previous crystal structures including
137 the P-Rex1 PH domain, this same surface formed extensive protein-protein lattice contacts (Cash
138 et al., 2016; Lucato et al., 2015). The residues directly involved in the interface are among the most
139 strongly protected in the presence of IP_4 as measured by HDX-MS (Fig. 1A-C, Sup. Fig. 4). The
140 PH domain β3/β4 loop, which we previously showed to be a nonspecific anionic membrane-
141 binding loop, remains unstructured and is situated near a loop at the tip of the 4HB that is also
142 unstructured (residues 1109-1209, Fig. 2C) and contains known phosphorylation sites, some of
143 which regulate activity (Barber et al., 2012). At the interface, surface hydrophobic residues Leu279
144 and Ile286 on the PH β1 and β2 strands and Tyr353 on the β5/β6 loop interact with a surface of
145 4HB including Tyr1096 and His1224 (Fig. 2D). Charge complementarity is formed between
146 Lys302 in the PH domain and Asp1216 in 4HB, and between the 1-phosphate of IP_4 and Lys1217.
147 Otherwise, IP_4 does not make direct contact with the 4HB. However, because different PH domain
148 ligands uniquely perturb the conformation of these regions in the PH domain (Cash et al., 2016),
149 IP_4 could indirectly stabilize this interface by trapping the β1 and β2 strands and β5/β6 loop in a
150 conformation with higher affinity for 4HB.

151 The jack-knife in the helix between the DH and PH domains is required to allow the PH
152 domain to interact with the 4HB and is stabilized by the DEP1 domain docking to the DH domain
153 (Fig. 2B). DH domain residues Leu173, Leu177, and Leu178 form a hydrophobic interface with
154 DEP1 residues Ile409, Ile457, Leu466, and Ala469 (Fig. 3A). Leu173 and Leu177 were previously
155 noted to be conspicuously exposed in structures of the DH/PH tandem (Cash et al., 2016). Thus,
156 the DEP1 domain stabilizes an inactive DH/PH tandem that is further stabilized by interaction with
157 the 4HB of the IP4P domain.
158 While conducting these studies, the structure of human P-Rex1 in the absence of IP_4 was
159 reported (PDB entry 7SYF) (Chang et al., 2022), allowing a comparison between the IP_4 and IP_4-
160 free states of autoinhibited P-Rex1. Overall, the domain organization is very similar, but there is
161 an ~3˚ rotation of the Gβγ-binding core in the IP_4 complex relative to the PH–4HB interface such
162 that DEP1 and DEP2 move closer together. It is possible that the binding of IP_4 at this interface
163 drives this conformational change. A caveat is that the protein used for the 7SYF structure
164 contained a T4 lysozyme domain inserted into the β3/β4 loop of the PH domain. Although this
165 domain was not visible in the reconstruction, its proximity to the IP_4 binding site may influence
166 the global conformation of P-Rex1. The similarities between P-Rex1±IP_4 also suggest that the IP_4-
167 binding site in the PH domain is freely accessible in the autoinhibited state. PIP_3 would, however,
168 not have access because the 4HB domain would block binding to a membrane surface.
169
170 *The DH–DEP1 interface contributes to autoinhibition in vitro.*
171 To test the contribution of the observed DH–DEP1 interface to autoinhibition, the interface was
172 disrupted by site-directed mutagenesis in the context of the DH/PH-DEP1 fragment. This fragment
173 is 5- to 10-fold less active (depending on assay conditions) than the DH/PH tandem alone (Sup.

Fig. 1C) (Ravala et al., 2020), confirming a specific role for DEP1 in autoinhibition (Fig. 3C). Single point mutations in the interface profoundly affected GEF activity on soluble Cdc42. The L173A variant had ~2.5-fold higher activity, whereas L177E and L178E exhibited 4- to 5-fold higher activity, similar to the activity of DH/PH without the DEP1 domain. In the DEP1 domain, I409A and L466A mutations resulted in ~2- and 4-fold higher activity, respectively. The α1/α2 loop (residues 77-90) of the DH domain, although ordered in previous structures of DH/PH bound to GTPases (Cash et al., 2016; Lucato et al., 2015), is disordered in our structure (Fig. 3B). However, modeling the DH domain from previous DH/PH crystal structures suggests that Lys89 and Arg78 would be close enough to form a bipartite ionic interaction with Glu456 in the DEP1 domain. Consistent with this hypothesis, the E456K variant was ~2.5-fold more active. Surprisingly, one of the intended disruptive mutations, A170K, instead inhibited GEF activity by ~50% (Fig. 3C). Based on our structure, Lys170 could form a salt bridge with DEP1 Glu411 in addition to forming non-polar interdomain contacts, stabilizing the DH–DEP1 interface (Fig. 3B).

The DH—DEP1 interface stabilizes DH/PH-DEP1 and decreases flexibility.

Because disruption of the DH–DEP1 interface led to increased activity, we predicted that these variants have a more extended DH/PH module that is likely more dynamic. To test this, wild-type (WT) DH/PH-DEP1 and its variants were assessed using a Thermofluor assay to determine their melting temperatures (T_m). Indeed, variants with increased activity also had lower T_m values (Fig. 3D, Table 2). Conversely, A170K, which was less active than WT, showed a higher T_m. We also analyzed these variants using size exclusion chromatography coupled to small-angle X-ray scattering (SEC-SAXS) (Sup. Fig. 5A&B). In previous SAXS analyses, we observed that DH/PH-DEP1 exhibited a more compact state with a smaller conformational landscape in solution relative

to DH/PH (Ravala et al., 2020). We hypothesized that mutations which disrupt the DH–DEP1 interface would likewise lead to more elongated ensembles. Compared to WT DH/PH-DEP1, which had a radius of gyration (R_g) of 30 ± 0.3 Å, the L177E variant (the most active DH/PH-DEP1 variant tested) had an R_g of 31 ± 0.2 Å, suggestive of expansion (Fig. 3E and Table 3). Variants A170K and I409A had R_g values similar to that of WT. Kratky plots indicated that all the samples had heterogeneous conformations (Sup. Fig. 5C). The shapes of the P(r) functions were similar for all variants except a longer tail for L177E and I409A, consistent with a higher proportion of extended conformations in solution (Sup. Fig. 5D).

Because the samples exhibited a high degree of heterogeneity in solution, the conformational distribution of these variants was assessed using the ensemble optimization method (EOM) (Fig. 3E&F, Sup. Fig. 5A) (Tria et al., 2015). The resulting ensemble for WT shows predominant conformations with R_g values ~ 28 Å and a small fraction of extended conformations with R_g ~ 39 Å (Fig. 3E). The selected ensemble for A170K had R_g values similar to WT (~29 Å), however the A170K peak is broader in comparison, suggesting conformational heterogeneity and structural changes. The L177E variant exhibited a larger shift to higher R_g, with an average R_g ~ 30 Å, and a second significant population with R_g > 32 Å (Fig. 3E). Similar to the distribution of R_g values, the D_{max} function distribution shows that the L177E variant had the most extended conformation of the variants tested (Fig. 3F). Other analyses were also consistent with L177E being the most flexible and extended variant (see methods).

The kink in the α6-αN helix of the DH/PH module is important for autoinhibition.

We hypothesized that the kink in the α6-αN linker of the DH/PH tandem is important for autoinhibition. If this is true, then introduction of disulfide bonds that lock this kinked

configuration should reduce activity. To test this, we used the DH/PH-DEP1 A170K variant as the backbone and created the S235C/M244C and K207C/E251C double mutants. Single cysteine variants K207C and M244C were also generated as controls. Both S235C/M244C and K207C/E251C variants exhibited reduced GEF activity that was reversed upon addition of DTT (Fig. 4B). However, the M244C variant displayed similar behavior, suggesting that disulfide bonds with cysteine(s) other than S235C were forming. Indeed, the side chains of Cys200 and Cys234 are in proximity to the M244C residue. The Lys207/Glu251 pair is interesting because these residues could form a salt bridge and stabilize the bent conformation. Mutating both residues to Cys had little effect on activity under non-reducing condition. However, under reducing conditions, K207C/E251C became ~15-fold more active, likely because the 207/251 residue pair was no longer restrained by a disulfide bond or a salt bridge. In total, these data support the idea that a kinked α6-αN hinge is important for autoinhibition of P-Rex1.

Interactions at the P-Rex1 DH–DEP1 and PH–4HB interfaces contribute to autoinhibition in cells. To evaluate the roles of the P-Rex1 DH–DEP1 and PH–4HB interfaces in living cells, we utilized SRE luciferase-gene reporter assays as a read out of full-length P-Rex1 activity in HEK293T cells. Mutations at the DH–DEP1 interface had a strong effect on activity, with L177E and L466E (Fig. 3A) exhibiting ~10-fold and ~4-fold higher activity relative to WT, respectively (Fig. 5A). Perturbation of the PH–4HB interface (Fig. 2D) also increased activity in that Y1096A was ~5-fold more active than WT (Fig. 5A). Mutation of other residues in the PH–4HB interface (Fig. 2D) also increased activity, although to a lesser extent.

The most affected variants (L177E, L466E, and Y1096A) were then tested for their effects on cell migration in response to chemokine gradients (Fig. 5B&C, Sup. Fig. 6A&B). For this, the

endogenous P-Rex1 gene in HeLa cells was first knocked out by CRISPR-Cas9 (Sup. Fig. 6C) and the resulting cells were transfected with various P-Rex1 constructs (Sup. Fig. 6D). Cell migration was then evaluated in the presence or absence of CXCL12 (upstream of P-Rex1 and Gβγ signaling) and epidermal growth factor (EGF). CXCL12-induced chemotaxis was dependent on the expression of P-Rex1 (Fig. 5B&C and Sup. Fig. 5), and all three variants caused a significantly larger number of cells to migrate. However, EGF-induced chemotaxis in HeLa cells, which is not dependent on P-Rex1, was unaffected by P-Rex1 expression. These data support that the DH–DEP1 and PH–4HB interfaces of P-Rex1 mediate autoinhibition that specifically modulates chemokine-induced cell migration.

P-Rex1 binding to PIP_3-containing model membranes induces a more open, dynamic conformation.

Given the known binding site for Gβγ (Cash et al., 2019), the position of membrane-binding loops such as the β1/β2 loop of the DEP1 domain (Ravala et al., 2020), and the position of the 4HB domain, it does not seem that the PH domain would be able to interact with PIP_3 in a cell membrane while P-Rex1 is in its autoinhibited conformation. To better understand the molecular consequences of PIP_3 binding, HDX-MS measurements were taken on P-Rex1 in the presence of liposomes ± PIP_3. Without PIP_3, the most notable changes in P-Rex1 in response to liposomes were increases in protection of the lipid binding elements of both DEP domains (primarily their β1/β2 loops; Sup. Fig. 7A, Sup. Data 2), which suggests that they directly interact with lipid bilayers. Indeed, the isolated DEP1 can independently bind negatively charged liposomes (Ravala et al., 2020). Within the PH domain, there was deprotection of the αC helix, but there was no deprotection at the PH–4HB interface, suggesting that it remained intact. In contrast, membranes

266 with PIP_3 caused deprotection of the entire DH domain, the α6-αN linker and the helices at the
267 DH–DEP1 interface (Fig. 6A, Sup. Fig. 6B, Sup. Data 2). Although the core of the PH domain
268 showed, as expected, an increase in protection in the presence of PIP_3, the structural elements
269 contacting 4HB became deprotected, as did the PH-binding regions of 4HB. Collectively, these
270 data are consistent with loosening of interdomain contacts and unraveling of at least some fraction
271 of P-Rex1 onto the surface of the liposome.
272
273 **Discussion**
274 Here, we showed that IP_4 binding to the PIP_3-binding site in full-length P-Rex1 stabilizes
275 a closed, autoinhibited conformation of P-Rex1 by enhancing long-range contacts across the length
276 of the protein. DH–DEP1 and PH–4HB interactions are relieved upon binding PIP_3-containing
277 liposomes, leading to activation of P-Rex1. Canonically, PIP_3 signaling is negatively regulated by
278 PIP_3 phosphatases such as PTEN. Additionally, inositol phosphates, including IP_7 and IP_4, can
279 compete with PIP_3 binding to PH domains (Jia et al., 2007), representing another form of negative
280 regulation. Ins(1,3,4,5)P_4 is a major isoform of IP_4 in neutrophils (Stuart et al., 1994) where its
281 concentration is estimated to be 4 μM (French et al., 1991) and where P-Rex1 is highly expressed
282 (Welch et al., 2002). Because we can measure significant inhibition of P-Rex1 by IP_4 at > 1 μM
283 (Fig. 1D), IP_4 may exert biologically relevant control of Rac activation, at least in neutrophils.
284 Since P-Rex1 can bind membranes in the absence of PIP_3 or Gβγ, IP_4 may serve to suppress P-
285 Rex1 activity until a threshold concentration of PIP_3 is generated, allowing rapid activation of
286 already cell membrane-associated P-Rex1. It is worth noting that this regulation by specific
287 inositol phosphates may depend on the intracellular distribution of the enzymes responsible for
288 their synthesis (Gokhale et al., 2011).

Another key result of our study was to provide a molecular explanation for how the PH and DEP1 domains contribute to P-Rex1 regulation. Nearly two decades ago, it was first reported that domains located C-terminal to the DH domain contribute to P-Rex1 autoinhibition (Hill et al., 2005). Deletion of the PH domain in P-Rex1 resulted in a large increase in activity in the context of the full-length enzyme. However, the DH/PH fragment has higher activity than DH/PH-DEP1 and larger P-Rex1 fragments, indicating that the PH domain itself is not intrinsically inhibitory, as it is in some other RhoGEF DH/PH tandems (Bandekar et al., 2019; Chen et al., 2020)(Ravala and Tesmer, 2023). This apparent contradiction can now be explained by the fact that in DH/PH-DEP1 and larger fragments, the DH/PH module can jack-knife and position the PH domain in a manner that blocks GTPase binding. This model of regulation was corroborated by recent structural studies of P-Rex1 without IP_4 (Chang et al., 2022). The isolated DEP1 domain was also shown to play an autoinhibitory role based on the relatively low activity of DH/PH-DEP1 relative to DH/PH (Ravala et al., 2020). This can now be explained by its interaction with the DH domain, which, consequently, positions the PH domain to block access of GTPases. Because the PH and DEP1 domains can mediate inhibition in the contexts of both DH/PH-DEP1 and the full-length enzyme, and because there is little GEF activity when DH–DEP1 interface is intact, the DH/PH-DEP1 module can be thought of as the core signaling circuit in P-Rex1. In support of this, our mutations in the DH–DEP1 interface were, in general, more activating than those in the PH–4HB interface in cells, although we note that our mutagenesis was not exhaustive (Fig. 5).

Using our functional data along with the known structures of P-Rex1, we assembled a model for the activation of P-Rex1 by PIP_3 and Gβγ (Fig. 6B). P-Rex1 in its basal state may be associated with IP_4 and exist in equilibrium at the membrane or in the cytosol. Indeed, in our HDX-MS studies, the DEP1 and DEP2 domains show protection in the presence of liposomes even

without PIP_3 (Sup. Fig. 7, Sup. Data 2). In its autoinhibited configuration, the known membrane anchoring elements (the GTPase binding site of the DH domain, the PIP_3-binding site of the PH domain, the β3/β4 loop of the PH domain, the β1/β2 loops of DEP1 and DEP2, and the Gβγ binding site in the C-terminal domains) cannot engage a common membrane plane (Fig. 6B). The clear outlier is the PH domain which would not be able to engage the membrane along with the other domains without unwrapping of the autoinhibited conformation. PIP_3 is not major driver of membrane anchoring on its own (Barber et al., 2007; Cash et al., 2016), and nor is Gβγ, but they do so synergistically in combination (Barber et al., 2007). In prior HDX-MS studies, Gβγ binding did not have a large effect on the regions now known to be involved in autoinhibition and only caused protection in regions of direct contact (Cash et al., 2019). This supports the idea that its role in activation may be primarily related to translocation. This is consistent with the observation that the ΔPH variant of P-Rex1 (which cannot form the DEP1–DH or PH–4HB interfaces or bind PIP_3) is activated to the same extent by Gβγ as WT P-Rex1 (Hill et al., 2005). In autoinhibited P-Rex1, the Gβγ binding site is readily accessible whereas that of PIP_3 is sequestered.

We propose that, after stimulation of GPCRs in neutrophils, Gβγ likely binds first and, with the assistance of membrane binding elements in the DEP1 and 2 domains and possibly the β3/β4 loop of the PH domain, promotes loosening of the autoinhibited state (Fig. 6B). Generation of PIP_3 by PI3K then releases the DH/PH module from the 4HB and DEP1 domain, displacing any bound IP_4. Because neither PIP_3 nor IP_4 can activate DH/PH-DEP1 GEF activity on a soluble GTPase (Sup. Fig. 1A&B), we speculate that this unwrapping at the membrane with multiple points of engagement across the protein is necessary for full activation of P-Rex1 (Fig. 6B). Indeed, our HDX-MS and SAXS studies here support that fully activated P-Rex1 at the membrane will be more extended and dynamic, making the DH domain more accessible to Rac1. However, what

remains unknown is the mechanism by which the PH domain is able to access PIP_3 at the membrane, even in a "loosened" autoinhibited state. Furthermore, additional layers of P-Rex1 regulation exist that remain underexplored. For example, phosphorylation of the lipid binding loop of DEP1 by PKA is known to inhibit P-Rex1 (Chávez-Vargas et al., 2016; Ravala et al., 2020). Also, a potential interaction may occur between the basic β3/β4 loop of the PH domain and the loop at the end of the 4HB (Fig. 2C). Both loops, consistent with their extended and dynamic nature, have predicted and confirmed phosphorylation sites (Barber et al., 2012) and thus could potentially modulate P-Rex1 activity if they interact. Phosphorylation of the basic β3/β4 loop might be expected to inhibit activity based on the fact that it binds and localizes the protein to the negatively charged plasma membrane, consistent with dephosphorylation of the loop leading to activation (Montero et al., 2016, 2013).

Materials and Methods

Cloning and site-directed mutagenesis

Full-length human P-Rex1, Cdc42 and DH/PH-DEP1 expression constructs were described previously (Cash et al., 2019, 2016; Ravala et al., 2020). Mutations in DH/PH-DEP1 were created using QuikChange (Qiagen) and confirmed by DNA sequencing. Mutations in the pCEFL-HA-HaloTag-P-Rex1 WT construct were created by QuikChange II site-directed mutagenesis (Agilent 200523). All constructs were confirmed by sequencing and expression was tested by immunoblot.

Protein purification

Full-length P-Rex1 was transiently expressed in Freestyle 293-F cells and purified as discussed previously (Cash et al., 2019). Briefly, 48 h after transfection, the cells were harvested and lysed

with Cell Lytic M (Sigma). After ultracentrifugation to remove the insoluble fraction, the protein was purified using glutathione agarose resin (Gold Biotechnology Inc.). The protein was subjected to TEV cleavage to remove the GST tag and then further purified using a Mono Q 5/50 GL anion exchange column (GE Healthcare Life Sciences). Finally, the protein was purified over an affinity column generated by conjugating human Rac1 to Affi-Gel 10 resin, although for Krios cryo-EM and HDX-MS experiments, this step was omitted.

P-Rex1 DH/PH-DEP1 proteins were expressed and purified as described previously (Ravala et al., 2020). Briefly, His-tagged protein was expressed in *E. coli* BL21(DE3) cells which were then lysed using an Avestin Emulsiflex-C3 high-pressure homogenizer. The cell lysate was clarified with high-speed centrifugation, the supernatant was collected, and protein was purified using Ni-NTA resin. The protein was subjected to TEV cleavage to remove the tag. The protein was then purified using a HiTrap SP sepharose column, concentrated, and subjected to size exclusion chromatography on a Superdex S75 column (GE Healthcare) column. Cdc42 was produced in an unprenylated form in *E. coli* and purified as previously described (Cash et al., 2016).

Hydrogen-deuterium exchange mass spectrometry

HDX-MS experiments were performed as previously described (Cash et al., 2019). Briefly, samples were mixed with D_2O buffer to initiate the HDX reaction and, at various time points, the reaction was quenched with ice cold quench buffer and the samples immediately frozen on dry ice. Samples were thawed at 4 °C and subjected to enzymatic digestion on an immobilized pepsin column followed by LC separation and MS analysis. Data were analyzed using HDExaminer (Sierra Analytics, LLC, Modesto, CA). Each sample was analyzed twice by HDX-MS, and the

data shown represent the average of these experiments. The average data of all five time points were used to plot the difference data onto the coordinates. Coordinates are colored using a range of -20% (darkest blue, protection) to 20% (darkest red, deprotection). P-Rex1 was used at a concentration of 1.7 mg/ml. IP_4 (Cayman Chemical) was added at a concentration of 100 µM. For experiments with liposomes, liposomes were added at a molar ratio of 1 P-Rex1 to 4000 total lipids. Liposomes were composed of 80:80:1 POPC:POPS:PIP_3 and prepared as previously described (Cash et al., 2019).

Guanine-nucleotide exchange assays

Proteins were evaluated for their GEF activity using a fluorescence-based assay (Cash et al., 2019). Briefly, N-methyl-anthraniloyl-GDP (mant-GDP) loaded soluble Cdc42 was used as a substrate GTPase (2 µM) in a buffer containing 20 mM HEPES pH 8, 100 mM NaCl, 0.5 mM $MgCl_2$, 100 µM GTP, and reactions were started by addition of P-Rex1 (100 nM). The loss of fluorescence was measured over time at 10 s intervals on a Flexstation 3 plate reader for 40 min. The data was fit to the one-phase exponential decay model in GraphPad Prism with the span (Y_o-plateau) shared among samples. For IP_4 competition curves, GEF assays were carried out in the presence of liposomes containing 2.5 µM PIP_3, as indicated, and 200 µM each of POPC and POPS, prepared as described previously (Cash et al., 2019).

Cryo-EM grid preparation and data collection

For cryo-EM sample preparation, P-Rex1 was used at a final concentration of 3 µM and *n*-dodecyl-β-D-maltoside (DDM) was added to a final concentration of 0.08 mM. For samples with IP_4, a final concentration of 40 µM IP_4 was added. A sample of 4 µl was applied to a glow-discharged Quantifoil (1.2/1.3) 300-mesh grid which was then blotted with filter paper and plunge-frozen into

liquid ethane cooled with liquid nitrogen using a Vitrobot Mark IV (Thermo Fisher Scientific) set to 4 °C, 100% humidity, 4 second blot, and a force of 10. Micrographs were collected either using Leginon (Suloway et al., 2005) on a Glacios transmission electron microscope (Thermo Fisher Scientific) operating at 200 keV and a K2 Summit direct electron detector (Gatan, Inc.) in counting mode (0.98 Å/pixel) at a nominal magnification of 45,000x or using EPU (Thermo Fisher Scientific) on a Titan Krios transmission electron microscope (Thermo Fisher Scientific) operating at 300 keV and a K3 direct electron detector (Gatan, Inc.) in counting mode (1.054 Å/pixel) at a nominal magnification of 81,000x. On the Krios, datasets were collected on both untilted and 30° tilted grids (Table 1).

Cryo-EM data processing

To overcome the severe preferred orientation problem of our sample on grids, we collected data on 0˚ and 30˚ tilted samples on a Krios electron microscope and processed these datasets separately up through 2D classification (Table 1). For each dataset, micrograph assessment, particle picking, and contrast transfer function estimation were performed using Warp (Tegunov and Cramer, 2019). Particle stacks were taken into CryoSPARC (Punjani et al., 2020, 2017) and extensively cleaned using 2D classification. A final merged particle stack was used for *ab initio* reconstruction into one class followed by non-uniform refinement to obtain a map at an overall 4.1 Å resolution for the P-Rex1·IP_4 complex. For Glacios datasets, data were processed only through 2D classification.

Model building and refinement

Initial model building relied on docking existing atomic models for the DH and PH domains of P-Rex1 (PDB entries 5FL1 and 5D3Y) and the Gβγ-binding scaffold (PDB entry 6PCV). 5D3Y was

used for the PH domain because the maps were consistent with IP_4 bound to the PIP_3 site of the PH domain. The DEP1 domain was placed using a non-domain swapped atomic model derived from PDB entry 6VSK. The linker between the PH and DEP1 domains and the 4HB domain were built by hand. A Dali search (Holm and Laakso, 2016) using backbone helices of 4HB revealed its topology to be similar to FAT domains, which was then used to adjust the register of each of its four helices. When Alphafold2 (Jumper et al., 2021) became available, it was used to further adjust the modeling of the 4HB domain and associated structural elements in the IP4P domain. Finally, when the cryo-EM structure of P-Rex1 (PDB entry 7SYF) and the crystal structure of the DH/PH-DEP1 module (PDB entry 7RX9) became available, they were used to confirm less certain regions. Final rounds of real space refinement iterating with manual building were performed in Phenix (Liebschner et al., 2019). Final structure statistics are given in Table 1, and the structure and associated maps were deposited as PDB entry 8TUA and EMDB entry EMD-41621. Raw data were deposited as EMPIAR entry XXXX.

Structure visualization

UCSF ChimeraX (Pettersen et al., 2021) was used to make figures showing cryo-EM maps. PyMOL (The PyMOL Molecular Graphics System, Version 2.5.5 Schrödinger, LLC) was used to create all other structure images.

Size exclusion chromatography coupled to small-angle X-ray scattering (SEC-SAXS)

For in solution characterization of DH/PH-DEP1 and its variants, SEC-SAXS was conducted at the BioCAT beamline (Sector18) at the Advanced Photon Source, Argonne National Laboratory using an AKTA Pure FPLC and a Pilatus3 X 1M detector. Purified proteins were injected onto a Superdex 200 Increase 10/300 column at a final concentration of 3-5 mg/ml in 20 mM HEPES,

pH 7, 300 mM NaCl, 2% glycerol, and elution from this column flowed into SAXS flow cell for X-ray scattering. Data were collected every 1 s with 0.5 s exposure times at room temperature using 12 KeV X-rays (1.033 Å wavelength) and a 3.67 m sample-to-detector distance. The achievable q range for this experimental setup was (0.0043-0.3546 Å).

SAXS Analysis

The scattering data were processed using BioXTAS RAW 1.6.3 software (Hopkins et al., 2017) (Sup. Fig. 5A) and used to determine the forward scattering I(0) and the radius of gyration, R_g via Guinier analysis (Sup. Fig. 5B). The Kratky plot showed proteins to be flexible (Sup. Fig. 5C) leading to unsuccessful rigid modeling efforts. However, use of the ensemble optimization method (EOM) within ATSAS/3.0.5-2 aided in generating ensembles representing distinct conformational states of the DH/PH-DEP1 fragment and its variants A170K, L177E, and I409A in solution at equilibrium (Ravala et al., 2020). For EOM, the models were generated using crystallographic coordinates from their respective crystal structures: PDB 5FI1 and PDB 6VSK. EOM generated 50,000 possible profiles for the full pool using default settings and native-like structures. From these profiles, a sub ensemble that matches the experimental scattering data is selected by a genetic algorithm run 10 times using default settings to verify the stability of the results (results from 1 run are shown in Fig. 3E&F). The pair distance distribution function P(r), which provides maximum particle dimension of each protein, was calculated using GNOM (DI, 1992) from the ATSAS 2.8.4 package (Franke et al., 2017) (Sup. Fig. 5D).

For quantitative analyses of the flexibility of the selected ensembles, R_{flex} and R_σ metrics were derived from EOM data. WT DH/PH-DEP1 and A170K show R_{flex} values smaller than those of the pools, which indicates that these proteins do not exhibit a fully flexible conformation. L177E and I409A variants exhibit R_{flex} values close to those of the pool, suggestive of being highly

flexible. Since Guinier analyses and the normalized residual fits of the proteins show that SAXS data quality is good (Sup. Fig. 5B), the R_σ value >1 is due to flexibility in the protein, consistent with the EOM analysis (Fig. 3E&F, Sup. Fig. 5A). Results of the SAXS analysis are presented in Table 3 in accordance with the revised guidelines for publishing SAXS data (Trewhella et al., 2017). The SAXS data are deposited in SASBD (https://www.sasbdb.org/) with access codes XXXX.

Differential scanning fluorimetry

Thermofluor experiments were performed on a QuantStudio 5 Real-Time PCR system in duplicate with n =3 independent experiments. Purified DH/PH-DEP1 and its variants were incubated at 1 mg/ml in a buffer containing 20 mM HEPES pH 7.0, 300 mM NaCl, and 2 mM DTT with 2.5x Sypro Orange dye in a final volume of 10 µl in a 384-well PCR plate. Fluorescence was monitored as a function of temperature, and the T_m was determined by fitting the fluorescence data to a sigmoidal curve and calculating the inflection point in GraphPad Prism.

Luciferase-gene reporter assay

HEK293T cells seeded in 12-wells plates coated with poly-D-lysine were transfected with 500 ng of empty vector pHTN HaloTag CMV-neo (Promega G7721) or pCEFL-HaloTag-P-Rex1 constructs and co-transfected with 500 ng of SRE-firefly luciferase and 50 ng of Renilla luciferase plasmids. Thirty-six hours after transfection, the cells were serum-starved overnight and then luminescence signal was measured using Dual-Glo assay system (Promega E2920) according to the manufacturer's instructions. Firefly-luminescence reads were normalized with Renilla-luminescence signal and adjusted to the negative control.

Preparation of P-Rex1 KO in HeLa cells and cell migration assays

HeLa cells were lentiviral transduced with pLentiCRISPRv2 P-Rex1 guide RNA3 - AGGCATTCCTGCATCGCATC (Genscript SC1678). Forty-eight hours after transduction, HeLa cells were selected with puromycin [3 µg/mL] for 7 days. P-Rex1 KO was confirmed by western blot. Chemotactic migration was measured by transwell assays (Thermoscientific 140629). Inserts of 24-well plates were pre-treated with Fibronectin [50 µg/mL] for 3 hours at 37 °C. Subsequently, $5x10^4$ HeLa cells prepared in serum-free DMEM were plated on the inserts at the upper chamber. Human CXCL12 [50 ng/mL] and EGF [50 ng/mL] (Sigma Aldrich SRP3276 and SRP6253) were prepared in serum-free DMEM and used as chemoattractant in the lower chamber. Serum-free DMEM was used as negative control. The plates with the inserts were incubated in a humidified atmosphere at 37 °C and 5% CO2 for 6 h. After incubation, the cells at the upper surface of the membrane insert were carefully removed and the cells attached to the lower surface were gently washed with PBS and then fixed with 4% paraformaldehyde for 15 min. After fixation, the cells were gently washed with PBS followed by staining with 0.5% crystal violet for 20 min. Excess of crystal violet was removed by gentle PBS washes. Migrating cells were imaged using an inverted microscope. Quantification of particles corresponding to migrating cells was performed with FIJI software.

Western blot

Protein samples prepared in Laemmli buffer were separated with SDS-PAGE using 4-12% gradient gels followed by transfer to PVDF membranes. The membranes were blocked using 5% non-fat milk in TBS-0.05% tween20 (TBST) and incubated overnight at 4 °C with primary antibodies against P-Rex1 and GAPDH (Cell signaling technology #13168 and #5174 respectively). The membranes were washed three times with TBST and then incubated with secondary antibodies in blocking solution for 2 h at room temperature. After washing three times

513 with TBST, the reactive bands were visualized using ECL detection reagents and CL-X-posure
514 films.

515 *Statistical analysis*

516 GEF assays described in this study were performed with n>=3 replicates. Statistical significance
517 was determined using one-way ANOVA test with a post hoc Dunnett's test for multiple
518 comparisons.

519 **Acknowledgements**

520 We thank Dr. Srinivas Chakravarthy, Beamline Scientist, for performing SEC-SAXS at BioCAT,
521 Chicago, IL and Dr. Jesse B. Hopkins, Deputy Director, BioCAT for help with SAXS data analysis
522 and interpretation. This research used resources of the Advanced Photon Source,
523 a U.S. Department of Energy (DOE) Office of Science User Facility operated for the DOE Office
524 of Science by Argonne National Laboratory under Contract No. DE-AC02-06CH11357. BioCAT
525 was supported by grant P30 GM138395 from the National Institute of General Medical Sciences
526 of the National Institutes of Health. We thank Dr. Thomas Klose in the Purdue Cryo-EM Facility
527 for technical assistance in cryo-EM data collection. Research reported in this publication was
528 supported by National Institutes of Health grants CA254402, CA221289, HL071818,
529 P30CA023168 (J.J.G.T.), by the Walther Cancer Foundation (J.J.G.T.), and by the National
530 Institute of General Medical Sciences of the National Institutes of Health grant R35GM146664
531 (J.N.C.).

532

533 **Table 1. Cryo-EM data collection, refinement, and validation statistics**

	Structure: P-Rex1–IP$_4$ (EMDB: EMD-41621) (PDB: 8TUA) (EMPIAR: xxxx)	
	Untilted	*Tilted*
Data collection		
Grids	Carbon Quantifoil	Carbon Quantifoil
Vitrification method	FEI Vitrobot	FEI Vitrobot
Microscope	Titan Krios	Titan Krios
Magnification	81000	81000
Voltage (kV)	300	300
Stage tilt (°)	0	30
Detector	K3 DED	K3 DED
Recording mode	Counting	Counting
Total electron exposure (e–/Å^2)	57.8	57.8
Number of frames	40	40
Defocus range (μm)	0.2 – 2.0	0.2 – 2.0
Pixel size (Å)	1.054	1.054
Data processing		
Number of micrographs	2,127	3,069
Initial particle images (no.)	806,067	1,620,545
Final particle images (no.)	89,450	119,739
Initial particle images merged (no.)	209,189	
Final total particle images (no.)	187,734	
Symmetry	C1	
Map resolution (Å)	4.1	
Refinement		
Initial model used (PDB code)	6PCV, 6VSK, 5D3X, 5FI1, 7RX9	
Model resolution (Å)	4.1	
FSC threshold	0.143	
Map sharpening *B* factor (Å^2)	-176	
Model composition		
Non-hydrogen atoms	10,685	
Hydrogens	10,709	
Protein residues	1,329	
Ligands	1 (4IP)	
B factors (Å^2; min/max/mean)		
Protein	35.3/201/117	
Ligand	137/137/137	
R.m.s. deviations		
Bond lengths (Å)	0.003	
Bond angles (°)	0.583	
Validation		
MolProbity score	1.74	
Clashscore	8.56	
Rotamer outliers (%)	0	
CaBLAM outliers (%)	1.97	
Ramachandran plot (%)		
Favored	96.0	
Allowed	4.0	
Outliers	0	

Model vs. Data	
CC mask	0.66
CC box	0.73
CC peaks	0.57
CC volume	0.66
Mean CC for ligand	0.64

534

535 **Table 2. Thermofluor measurements of DH/PH-DEP1 variants**

DH/PH-DEP1	T_m (°C)	
WT	44.0 ± 0.2	
A170K	45.4 ± 0.3	(p<0.0001)
L173A	43.0 ± 0.06	(p<0.0001)
L177A	43.4 ± 0.4	(p=0.0076)
L177E	43.4 ± 0.3	(p=0.0041)
L178A	43.1 ± 0.1	(p<0.0001)
L178E	42.9 ± 0.1	(p<0.0001)
I409A	41.7 ± 0.8	(p<0.0001)
E411K	43.9 ± 0.1	ns[b]
K415A	43.2 ± 0.5	(p=0.0047)
L451A	41.3 ± 0.5	(p<0.0001)
E456K	ND[a]	
L466A	ND	

From 2 independent experiments performed in triplicate.
P values are from one-way Anova comparisons with WT.
[a] ND: Not determined because inflection point not observed.
[b]ns: nonspecific.

536

Table 3. SAXS parameters for DH/PH-DEP1 variants

	WT	A170K	L177E	I409A
Guinier Analysis				
I(0)[a]	0.0081 ± 0.00004	0.0021 ± 0.003	0.0092 ± 0.00004	0.0034 ± 0.00002
R_g (Å)	30 ± 0.3	29 ± 0.08	31 ± 0.02	30 ± 0.4
Q_{min} ($Å^{-1}$)	0.0047	0.005	0.0047	0.0047
Q_{max} ($Å^{-1}$)	0.353	0.353	0.353	0.353
P(r) Analysis				
D_{max} (Å)	97	90	110	104
Volume ($Å^3$)	73900	75000	72500	74900
MM_{exp}(MM_{cal}) (kDa)	54 (54)	56 (54)	54 (54)	55 (55)
EOM Analysis				
Crystal Structures	5FI1;6VSK	5FI1;6VSK	5FI1;6VSK	5FI1;6VSK
q-Range ($Å^{-1}$)	.00475-0.353	0.00446-0.353	.00475-0.353	00475-0.353
R_{flex}	70.1% (82.6%)	71.9% (85.3%)	82.9% (84.9%)	79.1% (84.9%)
R_σ	1.18	0.60	1.08	1.56
Skewness	2.39 / 0.41	1.11/ 0.40	0.85 / 0.42	1.50/ 0.40
Kurtosis	4.86/ -0.08	2.09 / -0.14	-0.27 / -0.12	0.77 / -0.14

[a] SAXS parameters I(0), R_g, D_{max}, q_{min}, q_{max}, MMexp, MMcal, R_{flex}, R_σ are the experimentally determined intensity at zero scattering angle, radius of gyration, maximum particle dimension, minimum scattering angle, maximum scattering angle, molecular mass calculated from scattering data, molecular mass calculated based on amino acid sequence, flexibility metric of ensemble in comparison (pool value in parentheses), and ratio of standard deviation for the distribution of selected ensemble to that of pool, respectively. The values for EOM analysis are from the last run of the genetic algorithm.

References

Bandekar SJ, Arang N, Tully ES, Tang BA, Barton BL, Li S, Gutkind JS, Tesmer JJG. 2019. Structure of the C-terminal guanine nucleotide exchange factor module of Trio in an autoinhibited conformation reveals its oncogenic potential. *Sci Signal* **12**. doi:10.1126/scisignal.aav2449

Barber MA, Donald S, Thelen S, Anderson KE, Thelen M, Welch HCE. 2007. Membrane Translocation of P-Rex1 Is Mediated by G Protein beta Subunits and Phosphoinositide 3-Kinase. *Journal of Biological Chemistry* **282**:29967–29976. doi:10.1074/jbc.m701877200

Barber MA, Hendrickx A, Beullens M, Ceulemans H, Oxley D, Thelen S, Thelen M, Bollen M, Welch HCE. 2012. The guanine-nucleotide-exchange factor P-Rex1 is activated by protein phosphatase 1α. *The Biochemical journal* **443**:173–183. doi:10.1042/bj20112078

Cash JN, Davis EM, Tesmer JJG. 2016. Structural and Biochemical Characterization of the Catalytic Core of the Metastatic Factor P-Rex1 and Its Regulation by PtdIns(3,4,5)P 3. *Structure* **24**:730–740. doi:10.1016/j.str.2016.02.022

Cash JN, Urata S, Li S, Ravala SK, Avramova LV, Shost MD, Gutkind JS, Tesmer JJG, Cianfrocco MA. 2019. Cryo–electron microscopy structure and analysis of the P-Rex1–Gβγ signaling scaffold. *Sci Adv* **5**:eaax8855. doi:10.1126/sciadv.aax8855

Chang Y-G, Lupton CJ, Bayly-Jones C, Keen AC, D'Andrea L, Lucato CM, Steele JR, Venugopal H, Schittenhelm RB, Whisstock JC, Halls ML, Ellisdon AM. 2022. Structure of the metastatic factor P-Rex1 reveals a two-layered autoinhibitory mechanism. *Nat Struct Mol Biol* 1–7. doi:10.1038/s41594-022-00804-9

Chávez-Vargas L, Adame-García SR, Cervantes-Villagrana RD, Castillo-Kauil A, Bruystens JGH, Fukuhara S, Taylor SS, Mochizuki N, Reyes-Cruz G, Vázquez-Prado J. 2016. Protein Kinase A (PKA) Type I Interacts with P-Rex1, a Rac Guanine Nucleotide Exchange Factor. *Journal of Biological Chemistry* **291**:6182–6199. doi:10.1074/jbc.m115.712216

Chen M, Pan H, Sun L, Shi P, Zhang Y, Li L, Huang Y, Chen J, Jiang P, Fang X, Wu C, Chen Z. 2020. Structure and regulation of human epithelial cell transforming 2 protein. *Proc Natl Acad Sci* **117**:1027–1035. doi:10.1073/pnas.1913054117

Dorseuil O, Vazquez A, Lang P, Bertoglio J, Gacon G, Leca G. 1992. Inhibition of superoxide production in B lymphocytes by rac antisense oligonucleotides. *J Biol Chem* **267**:20540–20542. doi:10.1016/s0021-9258(19)36716-x

Franke D, Petoukhov MV, Konarev PV, Panjkovich A, Tuukkanen A, Mertens HDT, Kikhney AG, Hajizadeh NR, Franklin JM, Jeffries CM, Svergun DI. 2017. ATSAS 2.8: a

comprehensive data analysis suite for small-angle scattering from macromolecular solutions. *J Appl Crystallogr* **50**:1212–1225. doi:10.1107/s1600576717007786

French PJ, Bunce CM, Stephens LR, Lord JM, McConnell FM, Brown G, Creba JA, Michell RH. 1991. Changes in the levels of inositol lipids and phosphates during the differentiation of HL60 promyelocytic cells towards neutrophils or monocytes. *Proc R Soc Lond Ser B: Biol Sci* **245**:193–201. doi:10.1098/rspb.1991.0109

Gokhale NA, Zaremba A, Shears SB. 2011. Receptor-dependent compartmentalization of PPIP5K1, a kinase with a cryptic polyphosphoinositide binding domain. *Biochem J* **434**:415–426. doi:10.1042/bj20101437

Hayashi I, Vuori K, Liddington RC. 2002. The focal adhesion targeting (FAT) region of focal adhesion kinase is a four-helix bundle that binds paxillin. *Nat Struct Biol* **9**:101–106. doi:10.1038/nsb755

Hill K, Krugmann S, Andrews SR, Coadwell WJ, Finan P, Welch HCE, Hawkins PT, Stephens LR. 2005. Regulation of P-Rex1 by phosphatidylinositol (3,4,5)-trisphosphate and Gbetagamma subunits. *The Journal of biological chemistry* **280**:4166–4173.

Holm L, Laakso LM. 2016. Dali server update. *Nucleic Acids Res* **44**:W351–W355. doi:10.1093/nar/gkw357

Hopkins JB, Gillilan RE, Skou S. 2017. BioXTAS RAW: improvements to a free open-source program for small-angle X-ray scattering data reduction and analysis. *J Appl Crystallogr* **50**:1545–1553. doi:10.1107/s1600576717011438

Jia Y, Subramanian KK, Erneux C, Pouillon V, Hattori H, Jo H, You J, Zhu D, Schurmans S, Luo HR. 2007. Inositol 1,3,4,5-Tetrakisphosphate Negatively Regulates Phosphatidylinositol-3,4,5- Trisphosphate Signaling in Neutrophils. *Immunity* **27**:453–467. doi:10.1016/j.immuni.2007.07.016

Jumper J, Evans R, Pritzel A, Green T, Figurnov M, Ronneberger O, Tunyasuvunakool K, Bates R, Žídek A, Potapenko A, Bridgland A, Meyer C, Kohl SAA, Ballard AJ, Cowie A, Romera-Paredes B, Nikolov S, Jain R, Adler J, Back T, Petersen S, Reiman D, Clancy E, Zielinski M, Steinegger M, Pacholska M, Berghammer T, Bodenstein S, Silver D, Vinyals O, Senior AW, Kavukcuoglu K, Kohli P, Hassabis D. 2021. Highly accurate protein structure prediction with AlphaFold. *Nature* **596**:583–589. doi:10.1038/s41586-021-03819-2

Liebschner D, Afonine PV, Baker ML, Bunkóczi G, Chen VB, Croll TI, Hintze B, Hung L-W, Jain S, McCoy AJ, Moriarty NW, Oeffner RD, Poon BK, Prisant MG, Read RJ, Richardson JS, Richardson DC, Sammito MD, Sobolev OV, Stockwell DH, Terwilliger TC, Urzhumtsev AG, Videau LL, Williams CJ, Adams PD. 2019. Macromolecular structure determination using X-rays, neutrons and electrons: recent developments in Phenix. *Acta Crystallogr Sect D* **75**:861–877. doi:10.1107/s2059798319011471

Lucato CM, Halls ML, Ooms LM, Liu H-J, Mitchell CA, Whisstock JC, Ellisdon AM. 2015. The Phosphatidylinositol (3,4,5)-trisphosphate-dependent Rac Exchanger 1:Ras-related C3 Botulinum Toxin Substrate 1 (P-Rex1:Rac1) Complex Reveals the Basis of Rac1 Activation in Breast Cancer Cells. *Journal of Biological Chemistry*. doi:10.1074/jbc.m115.660456

Mayeenuddin LH, McIntire WE, Garrison JC. 2006. Differential sensitivity of P-Rex1 to isoforms of G protein betagamma dimers. *The Journal of biological chemistry* **281**:1913–1920. doi:10.1074/jbc.m506034200

Montero JC, Seoane S, García-Alonso S, Pandiella A. 2016. Multisite phosphorylation of P-Rex1 by protein kinase C. *Oncotarget* **7**:77937–77949. doi:10.18632/oncotarget.12846

Montero JC, Seoane S, Pandiella A. 2013. Phosphorylation of P-Rex1 at serine 1169 participates in IGF-1R signaling in breast cancer cells. *Cellular Signalling* **25**:2281–2289. doi:10.1016/j.cellsig.2013.07.018

Pettersen EF, Goddard TD, Huang CC, Meng EC, Couch GS, Croll TI, Morris JH, Ferrin TE. 2021. UCSF ChimeraX: Structure visualization for researchers, educators, and developers. *Protein Sci* **30**:70–82. doi:10.1002/pro.3943

Punjani A, Rubinstein JL, Fleet DJ, Brubaker MA. 2017. cryoSPARC: algorithms for rapid unsupervised cryo-EM structure determination. *Nat Methods* **14**:290–296. doi:10.1038/nmeth.4169

Punjani A, Zhang H, Fleet DJ. 2020. Non-uniform refinement: adaptive regularization improves single-particle cryo-EM reconstruction. *Nat Methods* **17**:1214–1221. doi:10.1038/s41592-020-00990-8

Ravala SK, Hopkins JB, Plescia CB, Allgood SR, Kane MA, Cash JN, Stahelin RV, Tesmer JJG. 2020. The first DEP domain of the RhoGEF P-Rex1 autoinhibits activity and contributes to membrane binding. *J Biol Chem* **295**:12635–12647. doi:10.1074/jbc.ra120.014534

Stuart JA, Anderson KL, French PJ, Kirk CJ, Michell RH. 1994. The intracellular distribution of inositol polyphosphates in HL60 promyeloid cells. *Biochem J* **303**:517–525. doi:10.1042/bj3030517

Suloway C, Pulokas J, Fellmann D, Cheng A, Guerra F, Quispe J, Stagg S, Potter CS, Carragher B. 2005. Automated molecular microscopy: The new Leginon system. *J Struct Biol* **151**:41–60. doi:10.1016/j.jsb.2005.03.010

Tegunov D, Cramer P. 2019. Real-time cryo–EM data pre-processing with Warp. *Nat methods* **16**:1146–1152. doi:10.1038/s41592-019-0580-y

Trewhella J, Duff AP, Durand D, Gabel F, Guss JM, Hendrickson WA, Hura GL, Jacques DA, Kirby NM, Kwan AH, Pérez J, Pollack L, Ryan TM, Sali A, Schneidman-Duhovny D, Schwede T, Svergun DI, Sugiyama M, Tainer JA, Vachette P, Westbrook J, Whitten AE.

2017. 2017 publication guidelines for structural modelling of small-angle scattering data from biomolecules in solution: an update. *Acta Crystallogr Sect D* **73**:710–728. doi:10.1107/s2059798317011597

Tria G, Mertens HDT, Kachala M, Svergun DI. 2015. Advanced ensemble modelling of flexible macromolecules using X-ray solution scattering. *IUCrJ* **2**:207–217. doi:10.1107/s205225251500202x

Urano D, Nakata A, Mizuno N, Tago K, Itoh H. 2008. Domain-domain interaction of P-Rex1 is essential for the activation and inhibition by G protein betagamma subunits and PKA. *Cellular Signalling* **20**:1545–1554. doi:10.1016/j.cellsig.2008.04.009

Welch HCE, Coadwell WJ, Ellson CD, Ferguson GJ, Andrews SR, Erdjument-Bromage H, Tempst P, Hawkins PT, Stephens LR. 2002. P-Rex1, a PtdIns(3,4,5)P3- and Gbetagamma-regulated guanine-nucleotide exchange factor for Rac. *Cell* **108**:809–821.

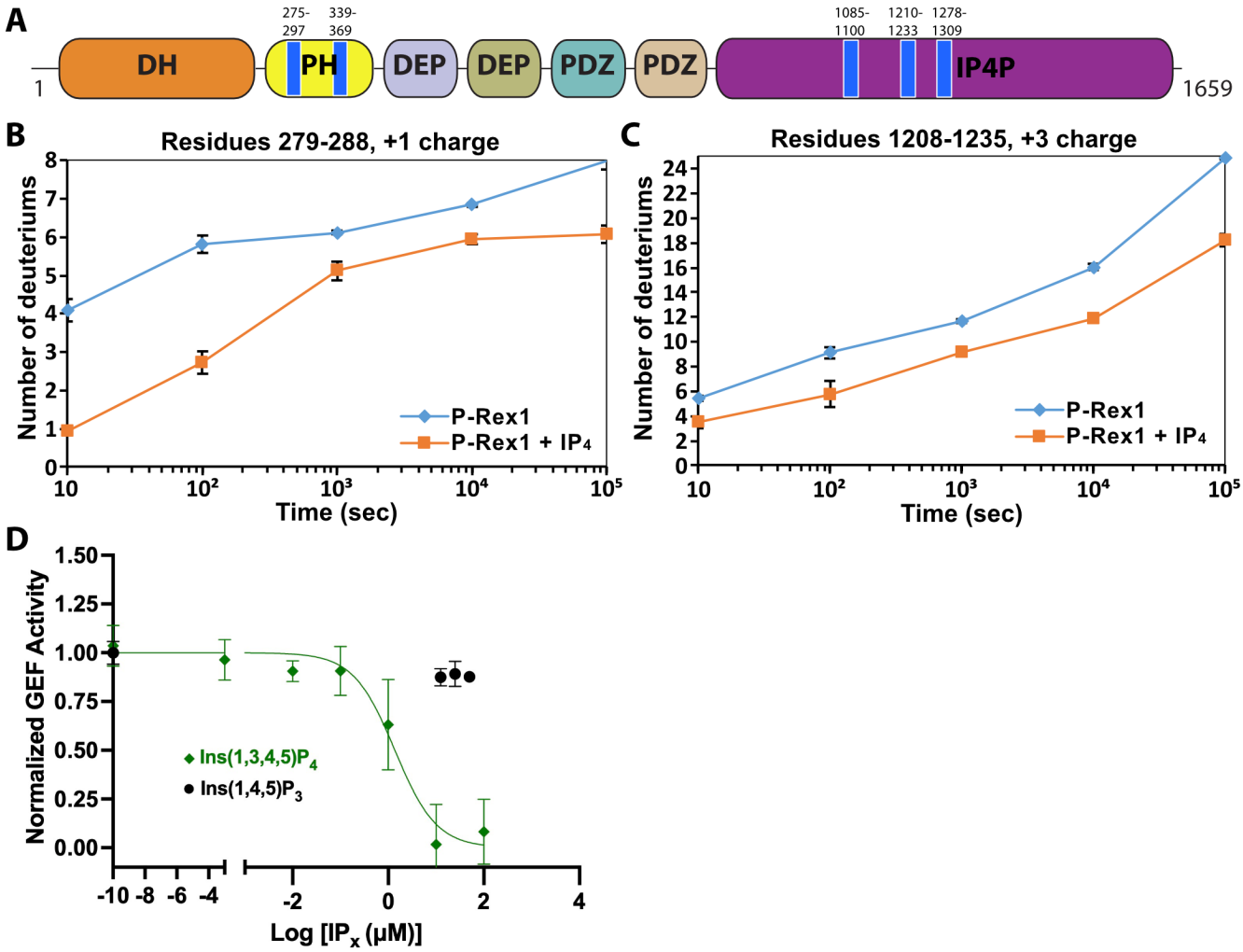

Figure 1. IP_4 binding causes dynamic changes in multiple domains of P-Rex1 and inhibits PIP_3-induced activation. A) Difference HDX-MS data plotted onto the domain layout of P-Rex1. Blue regions indicate less deuterium uptake upon IP_4 binding. Graphs show the exchange over time for select regions in the P-Rex1 (B) PH domain and (C) a IP4P region that was disordered in the P-Rex1–Gβγ structure. Error bars represent mean ± S.D. D) *In vitro* GEF activity of P-Rex1 evaluated on liposomes containing 2.5 μM PIP_3 in the presence of varying IP_4 concentrations (0-100 μM). Data were fit to exponentials to get rate constants by constraining the span to be shared. The resulting rates for each experiment were normalized by averaging two PIP_3 data points and two PC/PS data points to represent the top and bottom of the binding curve. The resulting normalized rates (min^{-1}) were fit with a one-phase binding curve wherein the top and bottom were constrained to 1 and 0, respectively, and the Hill coefficient fixed at -1. The resulting IC_{50} was 1.4 μM with a confidence interval of 0.81 to 2.3. Data represent 4-5 independent experiments. Error bars represent the mean ± S.D.

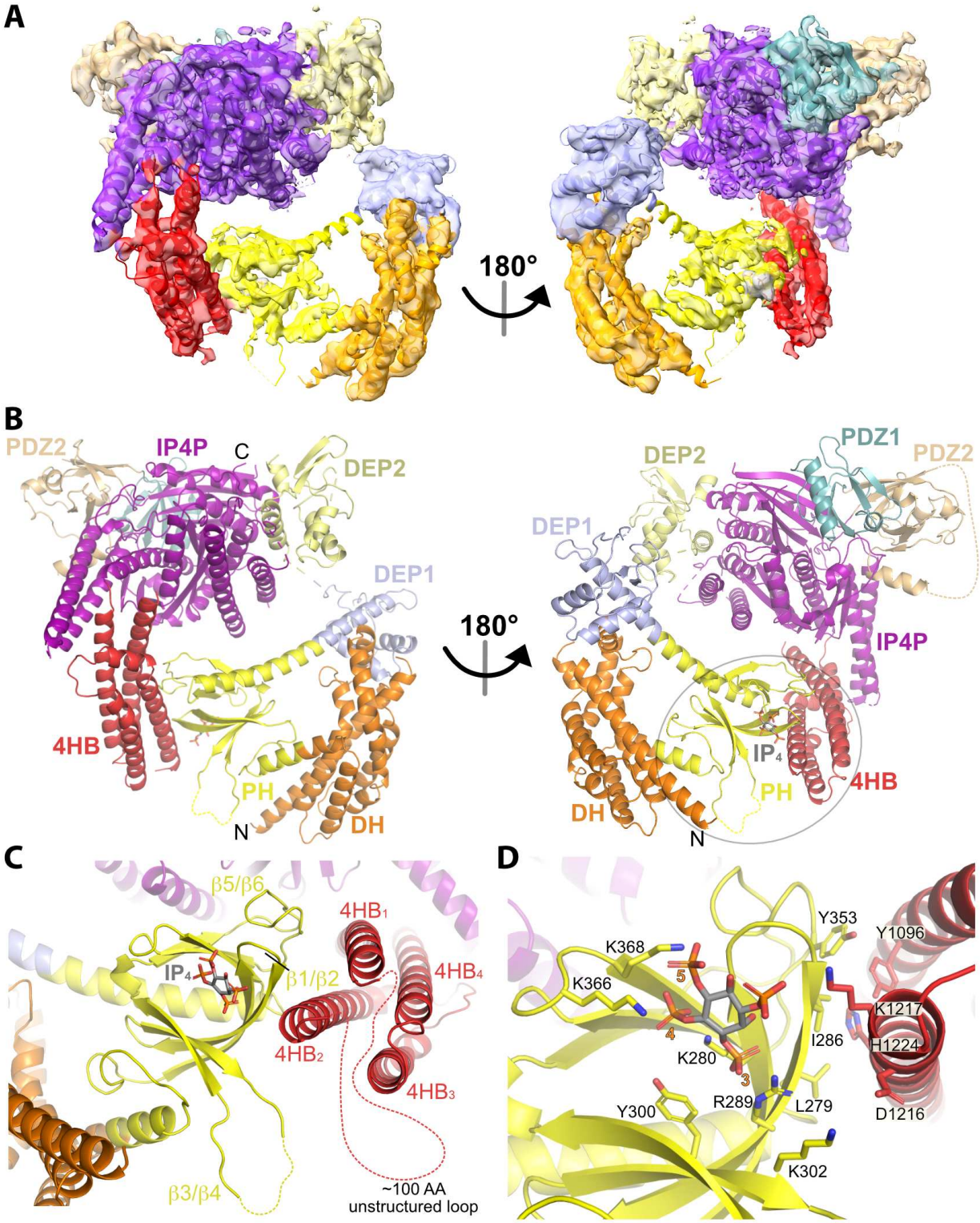

Figure 2. Structure of the P-Rex1·IP_4 complex in an autoinhibited conformation. A) Cryo-EM reconstruction with atomic model superimposed. B) Atomic model without the cryo-EM map. C) The PH–4HB interface primarily involves the β1/β2 and β5/β6 loops of the PH domain, which were previously shown to be involved in protein-protein interactions in crystal structures (Cash et al., 2016), and the $4HB_1$ and $4HB_2$ helices of the 4HB domain. Flexible loops, including the basic β3/β4 loop of the PH domain involved in membrane binding (Cash et al., 2016), are shown as dashed lines. We speculate that this loop could interact with phosphorylated residues in the adjacent 4HB unstructured loop. D) Side chains in the PH–4HB interface. The 3-, 4-, and 5-position phosphates of bound IP_4 are labeled. Note that PIP_3 could not bind to the PH domain in this state due to steric blockade by the 4HB domain. The area of focus in (C) and (D) is circled in transparent grey in (B).

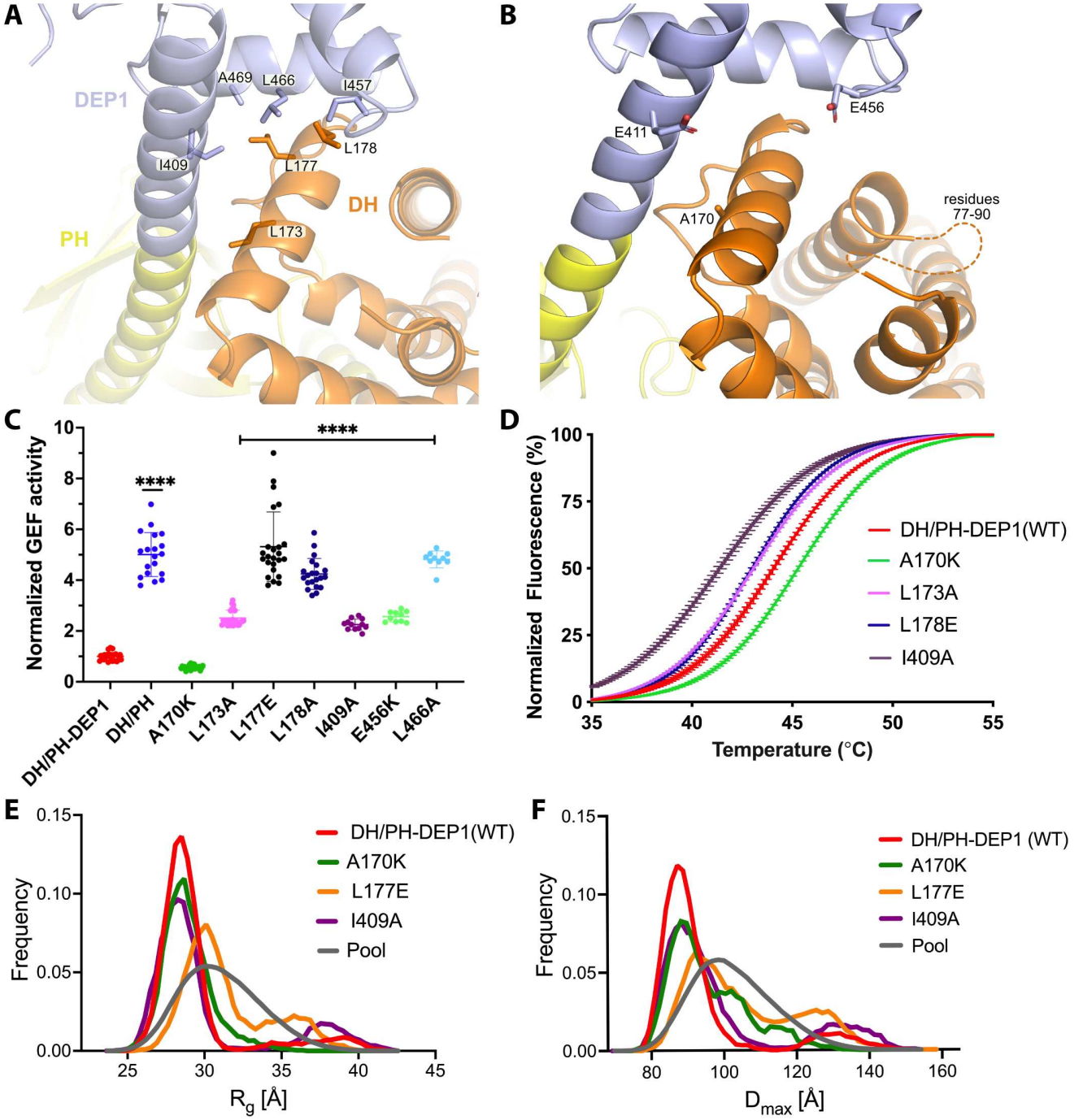

Figure 3. Mutations at the DH–DEP1 interface alter stability, conformation, and activity of DH/PH-DEP1. A) Side chains that contribute to the hydrophobic interface formed between the DH and DEP1 domains. B) Electrostatic interactions contributing the DH–DEP1 interface. The dotted line indicates a disordered region on the DH domain containing positively charged residues that may interact with Glu456. The A170K mutant is expected to form a salt bridge with Glu411 and strengthen the interface. C) Fluorescence based *in vitro* GEF activity assay on soluble Cdc42 with variants of the purified DH/PH-DEP1 fragment. GEF activity in this experiment was fit to a one phase exponential decay normalized to that of DH/PH-DEP1 (WT). ****, P<0.0001. D) Representative Thermofluor analyses showing that mutations that disrupt the DH–DEP1 interface also destabilize the protein, as evidenced by decreased T_m values for each variant (see **Table 2**). Data are normalized from 0-100% representing lowest and highest fluorescence values. Note that A170K, which inhibits activity in panel C, increases stability. E, F) EOM analysis of SAXS data collected from mutations disrupting the DH–DEP1 interface indicate that these variants exhibit more extended conformations (see **Table 3**). EOM analyses provide the R_g and D_{max} distributions derived from selected ensembles. The gray curves correspond to the R_g and D_{max} distributions for the pool of structures used for each analysis.

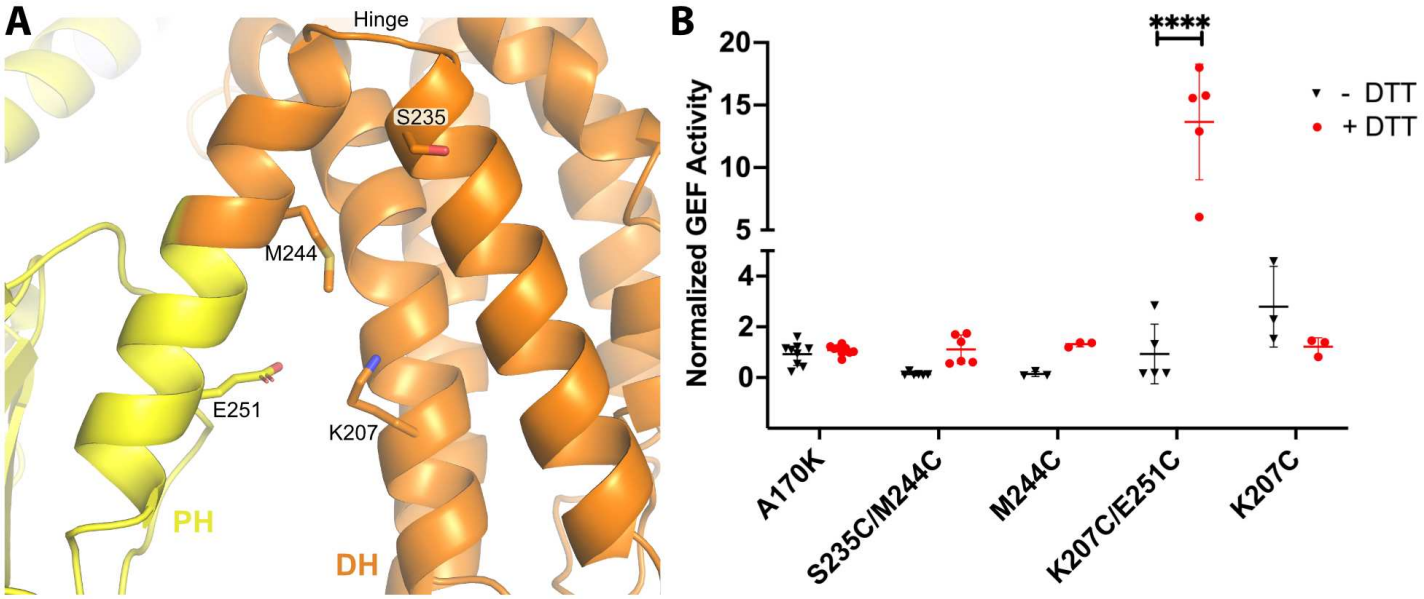

Figure 4. Introduction of a disulfide bridge in the DH/PH hinge reduces DH/PH-DEP1 activity. A) Atomic structure of the hinge between the DH and PH domains. Side chains of residues mutated to cysteine are shown. B) GEF activity of DH/PH-DEP1 Cys variants in the background of the A170K mutation. The rate of nucleotide exchange on soluble Cdc42 was normalized to that of the A170K DH/PH-DEP1 variant. Residues were mutated and activities measured under reducing (+DTT) and non-reducing (-DTT) conditions. Similar results were obtained when using $FeCN_6^-$ as an alternative oxidation strategy (data not shown). Data are from at least three independent experiments with error bars representing the mean ± S.D. ****, P<0.0001.

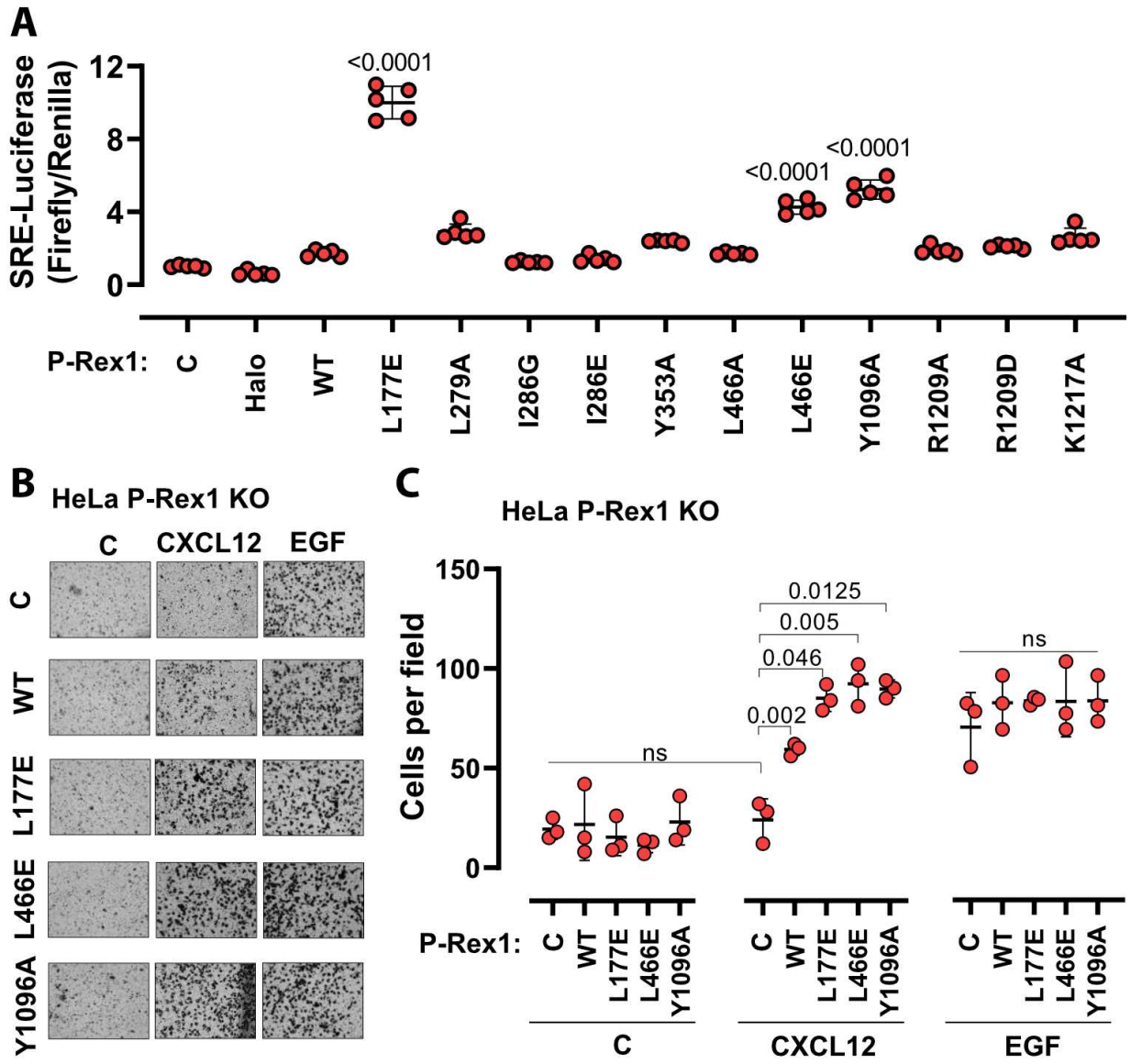

Figure 5. Disruption of the DH–DEP1 and PH–4HB interfaces leads to increased P-Rex1 activity in cells. A) SRE luciferase-gene reporter assays. Mutations were cloned into full-length P-Rex1 in the pCEFL-HA-HaloTag vector, and these constructs, along with luciferase reporter genes, were co-transfected into HEK293T cells. Results depicted here are representative of three independent experiments, and error bars represent S.D. Non-transfected control (C) and empty vector transfected control (Halo) are shown. B) Mutations which led to enhanced P-Rex1 activity in luciferase reporter assays were evaluated for their effect on chemotaxis of HeLa cells with endogenous P-Rex1 knocked out (HeLa P-Rex1 KO; see Supplemental Figure 5). P-Rex1 constructs were transfected into HeLa P-Rex1 KO cells, and cell migration was evaluated upon stimulation with CXCL12 (50 ng/ml) or EGF (50 ng/ml). Data is presented as mean ± S.D. Significance (brackets) was determined using multiple comparison ANOVA followed by Šidák statistic test.

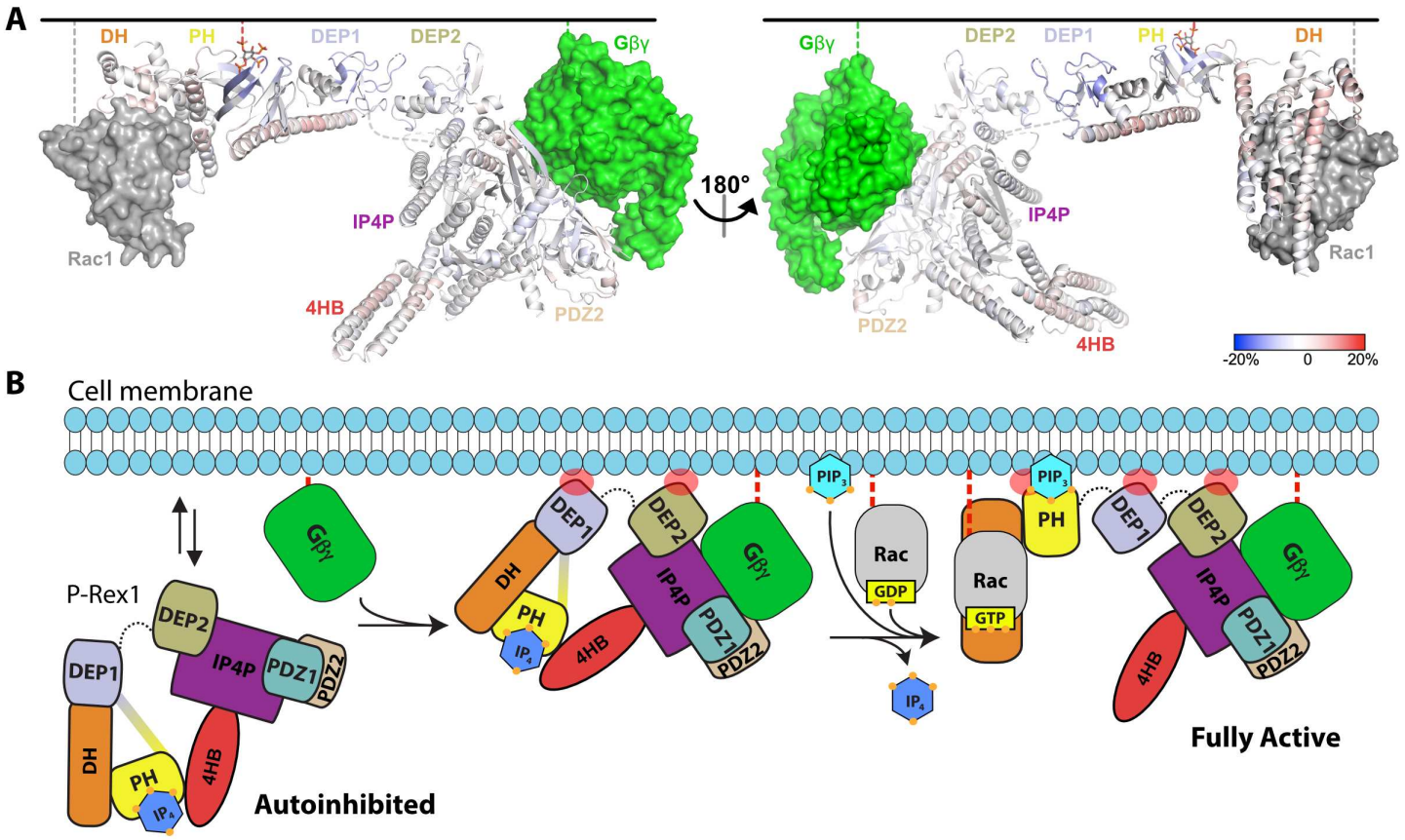

Figure 6. HDX-MS supports that P-Rex1 undergoes long range conformational changes when binding PIP_3-containing liposomes. A) HDX-MS of P-Rex1 in the presence of PIP_3-containing liposomes. A model of P-Rex1 in an open conformation bound to a membrane containing PIP_3 was created and is shown colored according to difference HDX-MS data plotted onto the coordinates. HDX-MS data was collected in the presence of liposomes containing PIP_3 and compared to data collected on P-Rex1 alone. Blue and red regions indicate less and more protection, respectively, upon PIP_3-containing liposome binding. These changes occur specifically in the presence of PIP_3 (see Supplemental Fig. 7). The black line at the top represents a membrane surface and the dashed lines represent covalent lipid modifications. Using available structural information, Gβγ and Rac1 were docked into this model (although neither were present in this HDX-MS experiment). B) Cartoon schematic of our model of the steps involved in the activation of P-Rex1.